Nanoscale Advances

ROYAL SOCIETY OF CHEMISTRY

PAPER

View Article Online
View Journal | View Issue

Cite this: *Nanoscale Adv.*, 2025, **7**, 2182

BSA@IR780-loaded mesoporous polydopamine nanoparticles with enhanced photostability for multimodal imaging and photothermal therapy of tumors†

Shuaibo Yang,‡[ab] Yanzhao Diao,‡[b] Lifeng Hang,[b] Hong Qu,[b] Laiping Fang,[b] Wei Guo,[ab] Hua Wen,[b] KuokWai Iu,[d] Guihua Jiang,*[b] Lianyi Shao*[a] and Quan Li*[c]

Multifunctional phototherapy that integrates diagnostic and therapeutic modalities holds the potential to revolutionize cancer treatment. The near-infrared cyanine dye IR780 is known for its high spatial resolution imaging capabilities. When conjugated with bovine serum albumin (BSA), it effectively mitigates common challenges such as photobleaching and fluorescence quenching, making it widely used in tumor imaging. However, its limited photothermal conversion efficiency hinders its broader application in tumor therapy. To overcome these limitations, this study presents the design and development of an imaging-guided multifunctional nanoplatform: mesoporous polydopamine (MPDA)-BSA@IR780. Our findings demonstrate that MPDA, as a carrier, significantly improves the photostability of BSA@IR780. Furthermore, MPDA's superior photothermal properties enhance the photothermal efficacy of the platform, enabling MPDA-BSA@IR780 to function as a dual photothermal therapy (PTT) agent. In addition to its therapeutic potential, MPDA-BSA@IR780 serves as both a photoacoustic (PA) and fluorescence (FL) imaging probe, effectively guiding treatment decisions. Cellular assays reveal that MPDA-BSA@IR780 exhibits a robust photothermal effect, supporting promising therapeutic outcomes. *In vivo* studies further demonstrate that, following laser irradiation, MPDA-BSA@IR780 achieves near-complete tumor ablation without inducing significant toxicity, while also exhibiting excellent biocompatibility. In conclusion, this study introduces a safe and effective photothermal nanoparticle platform for tumor imaging, diagnosis, and treatment, providing a promising strategy for future biomedical applications.

Received 2nd January 2025
Accepted 18th February 2025

DOI: 10.1039/d5na00008d

rsc.li/nanoscale-advances

Introduction

Phototherapy diagnostics have attracted increasing attention in recent years due to their potential to combine real-time diagnostic capabilities with localized treatment. Unlike traditional methods, phototherapy offers a non-invasive approach with minimal side effects, making it a promising strategy for cancer treatment.[1–3] Photothermal therapy (PTT), in particular, has gained significant interest in tumor research for its low toxicity, excellent controllability, and high selectivity.[4,5] PTT utilizes photothermal agents (PTAs) that absorb energy from an external light source and convert it into heat, inducing cancer cell death.[6–8] Among various light sources, near-infrared (NIR) light is the most commonly employed in PTT due to its superior tissue penetration, resulting in better therapeutic effects in deeper tissues with less biological interference.[9] As a result, NIR-responsive photothermal materials have become widely utilized in cancer treatment.[10]

NIR photothermal materials can be classified into inorganic and organic categories. Inorganic materials, such as carbon-based nanomaterials,[11] and transition metal sulfides,[12] have shown promise but are limited by concerns over cytotoxicity due to their poor biodegradability.[13] Organic photothermal nanomaterials have gained increasing attention in PTT due to their tunable structural and photophysical properties, high molar extinction coefficients in the NIR region, and excellent

[a]*School of Materials and Energy, Guangdong University of Technology, Guangzhou 510006, China. E-mail: shaolianyi@gdut.edu.cn*

[b]*The Department of Medical Imaging, Guangzhou Key Laboratory of Molecular Functional Imaging and Artificial Intelligence for Major Brain Diseases, The Affiliated Guangdong Second Provincial General Hospital of Jinan University, Guangzhou 518037, P. R. China. E-mail: jianggh@gd2h.org.cn*

[c]*Guangzhou Women and Children's Medical Center, Guangzhou Medical University, Guangdong Provincial Clinical Research Center for Child Health, Guangzhou, 510623, China. E-mail: huayu_3203@163.com*

[d]*Department of Diagnostic Imaging Center, Kiang Wu Hospital, Macau, 999078, China*

† Electronic supplementary information (ESI) available. See DOI: https://doi.org/10.1039/d5na00008d

‡ The authors contributed equally to this work.

biocompatibility.[14] On the other hand, organic photothermal nanomaterials, including small organic molecules and polymers, offer several advantages: tunable structural and photophysical properties, high molar extinction coefficients in the NIR region, and excellent biocompatibility. Organic materials, such as cyanine dyes, have been widely explored for their potential in PTT. However, the use of free cyanine dyes is limited by challenges such as strong hydrophobicity, poor photostability, self-quenching effects, and potential side effects.[15,16] Therefore, strategies to overcome these limitations are crucial for enhancing the potential of cyanine dyes in cancer diagnosis and therapy.

One promising solution involves covalently binding cyanine dyes to specific domains of albumin, forming a stable albumin-dye complex that can be used for tumor imaging.[17,18] Albumin, as a carrier, can prolong the circulation time of the dye molecules *in vivo*, leading to a stable and durable imaging probe.[19] The albumin@dye complex also enhances the brightness and quantum yield (QY) of the dye,[18,20] reduces self-quenching,[18] extends the imaging duration,[18] and improves solubility.[20] While the albumin@dye complex holds promise as a long-term imaging probe in fluorescence imaging, its limited photothermal conversion efficiency restricts its use in tumor therapy. Therefore, developing strategies to enhance the photothermal efficacy of albumin@dye complex is essential for better integrating phototherapy with diagnostics.

Polydopamine (PDA), a widely used biomaterial, has gained attention for its potential in drug delivery systems and photothermal therapy. However, due to limited efficacy, mesoporous polydopamine nanoparticles (MPDA), which possess an inherent porous structure and enhanced photothermal properties, have garnered increasing interest in cancer diagnosis and therapy.[21,22] Studies have shown that MPDA nanoparticles not only enable effective drug delivery but also exhibit remarkable photothermal conversion abilities,[23,24] making them ideal candidates for integrating photothermal therapy with diagnostic imaging.

In this study, we explore the development of a multifunctional diagnostic nanoplatform using MPDA as the carrier. Bovine serum albumin (BSA) was conjugated with the cyanine dye IR780 to form a BSA@IR780 complex. This complex was then loaded onto the MPDA nanoparticles, resulting in the formation of the MPDA-BSA@IR780 nanoplatform. The MPDA-BSA@IR780 nanoplatform offers several key advantages: (1) Enhanced photostability: MPDA improves the photostability of the BSA@IR780 complex, enhancing its effectiveness in both photothermal therapy and fluorescence imaging. (2) Improved photothermal effect: MPDA's strong photothermal properties address the limited photothermal response of BSA@IR780, thereby enhancing the therapeutic efficacy in tumor treatment. When exposed to an 808 nm laser, the MPDA-BSA@IR780 nanoplatform induces thermal ablation of tumors both *in vitro* and *in vivo*, while ensuring biosafety. By integrating diagnostics with therapy, the MPDA-BSA@IR780 nanoplatform not only improves treatment precision but also enhances antitumor effects, fully leveraging the potential of imaging-guided photothermal therapy.

Experimental

Materials

Dopamine hydrochloride (DOPA, 99%) was purchased from Aladdin Reagent Co. Pluronic® F-127 (F127, 98%) and IR780 were obtained from Sigma-Aldrich Co. LLC (USA). Dulbecco's Modified Eagle's Medium (DMEM) and fetal bovine serum (FBS) were purchased from BasalMedia (Shanghai, China). Trypsin–EDTA and penicillin–streptomycin were sourced from Solarbio (Shanghai, China). The Cell Counting Kit (CCK-8) was purchased from GEN-VIEW SCIENTIFIC Inc. (USA). PBS buffer (pH 7.4) was obtained from Zsbio (Beijing, China). The Calcineurin AM/PI live/dead assay kit was purchased from Shanghai Beyotime Biotechnology Institute. All chemicals are analytical grade and were used without further purification. Deionized water was used in all experiments.

Cells and animals

Mouse breast cancer cells (EMT6) and human normal lung epithelial cells (Beas2b) were obtained from the Cell Bank of the Chinese Academy of Sciences (Shanghai, China). Both cell lines were cultured in Dulbecco's Modified Eagle Medium (DMEM) (BasalMedia, Shanghai, China), supplemented with 10% (v/v) fetal bovine serum (FBS) (BasalMedia, Shanghai, China) and 1% (v/v) penicillin/streptomycin (Solarbio, Shanghai, China). The cells were maintained in a humidified incubator at 37 °C with 5% CO_2. For the animal experiments, 6–8 weeks-old female BALB/C mice were used. The mice were purchased from Zhuhai Biotest Biotechnology Co. (Zhuhai, China) and housed in the animal facility of the Affiliated Guangdong Second Provincial General Hospital of Jinan University under standard conditions. The animals were kept on a 12 hours light/dark cycle, with an ambient temperature of 22 ± 2 °C and relative humidity maintained between 40 and 60%. All animal handling and experimental procedures were approved by the Experimental Animal Management Committee of the Affiliated Guangdong Second Provincial General Hospital of Jinan University (Permit Number: 2023-DW-KZ-074).

Synthesis of MPDA NPs, BSA@IR780, MPDA-BSA@IR780 NPs

The MPDA NPs was synthesized by a reported process.[25] F127 (0.1 g), dopamine hydrochloride (0.15 g), ultrapure water (5 mL), and ethanol (5 mL) were mixed and sonicated to dissolve and disperse the components into a uniform solution. Then, 200 μL of homotrimethylbenzene was added to the solution, followed by further sonication to ensure the formation of a homogeneous mixture. Next, an alkaline solution of ammonia (375 μL) was added, triggering the polymerization of dopamine into polydopamine (PDA). The reaction mixture was stirred at room temperature for 2 hours to allow for complete polymerization. After polymerization, the product was collected by centrifugation (13 000 rpm, 15 min). The solid was washed three times: once with ethanol and twice with ultrapure water. The collected precipitate was then dispersed in a mixed solution of ethanol and ultrapure water (5 mL each). This dispersion was transferred to an autoclave reactor and heated at 100 °C for 24 hours.

Following the hydrothermal treatment, the product was again collected by centrifugation, and the final product, black MPDA nanospheres, was obtained by vacuum drying.

BSA@IR780 was prepared following a previously reported procedure.[26] BSA was dissolved in phosphate-buffered saline (PBS) at a concentration of 200 μM, and IR780 was dissolved in dimethyl sulfoxide (DMSO) at a concentration of 20 mM. Next, 50 μL of the 20 mM IR780 solution was added to 5 mL of the 200 μM BSA solution, achieving a dye-to-protein molar ratio of 1 : 1, meaning one IR780 dye molecule per BSA molecule. The mixture was then incubated in a constant-temperature water bath oscillator at 50 °C for 2 hours. After the reaction, the resulting product was BSA@IR780.

To prepare MPDA-BSA@IR780 nanoparticles, MPDA was first dispersed in deionized (DI) water and sonicated to ensure uniform distribution of the nanoparticles in the solution. Subsequently, 1 mL of BSA@IR780 solution was added to the MPDA dispersion, resulting in the formation of MPDA-BSA@IR780 nanoparticles. The mixture was then stirred mechanically in the dark for 12 hours. After stirring, the solution was centrifuged to isolate the formed MPDA-BSA@IR780 nanoparticles. Finally, the nanoparticles were stored at 4 °C for future use.

Characterization

Absorption spectra were recorded using a UV-3600 UV-vis spectrophotometer (Shimadzu, Japan). Fluorescence emission spectra were measured on an FS5 fluorescence spectrophotometer (Edinburgh Instruments, UK) with an excitation wavelength of 764 nm and a slit width of 3 nm. Emission was scanned over the wavelength range of 780–900 nm with a slit width of 2.5 nm. The size distribution and zeta potential of the nanoparticles were determined using a Zetasizer Nano-ZS (Malvern, UK). Morphological and microstructural analysis of the nanoparticles was conducted using a Tecnai G20 transmission electron microscope (FEI, USA) at an accelerating voltage of 200 kV and a Hitachi scanning electron microscope (Hitachi, Japan) at an accelerating voltage of 3 kV.

In vitro fluorescent properties

Fluorescence performance was evaluated by recording emission spectra using an Edinburgh Instruments FS5 spectrometer, with excitation provided by a 764 nm laser. The emission spectra of IR780 and BSA@IR780, both at the same concentration, were measured in the range of 780–860 nm. Additionally, the fluorescence spectra of MPDA-IR780 and MPDA-BSA@IR780 were assessed, with MPDA serving as the control group. To evaluate fluorescence stability, the emission spectra were recorded every minute during continuous laser irradiation (808 nm, 1 W cm^{-2}), and the fluorescence intensity decay of IR780, BSA@IR780, and MPDA-BSA@IR780 was compared.

In vitro photothermal properties

The photothermal conversion performance was assessed by irradiating pure water, MPDA, and MPDA-BSA@IR780 solutions for 5 minutes using a near-infrared laser (808 nm, 1 W cm^{-2}), with pure water serving as the control. Subsequently, a 300 μg mL^{-1} solution of MPDA-BSA@IR780 was irradiated for 5 minutes under varying power densities (0.5 W cm^{-2}, 0.75 W cm^{-2}, and 1 W cm^{-2}). Additionally, different concentrations of MPDA-BSA@IR780 (100, 200, 300, and 400 μg mL^{-1}) were irradiated for 5 minutes. Temperature changes were monitored and recorded throughout the experiments using a FLUKE Ti32 thermal imaging camera (Fluke, USA). The photothermal stability of MPDA-BSA@IR780 and MPDA-IR780 was evaluated under four laser irradiation on/off cycles (4 minutes of irradiation followed by a 3 minutes pause). The photothermal conversion efficiency (η) was calculated using the following equation.

$$\eta = \frac{hs(T_{max} - T_{sur}) - Q_{dis}}{I\left(1 - 10^{-A_{808}}\right)}$$

$$hs = \frac{m_i c_{H_2O}}{\tau_s}$$

$$Q_{dis} = hs(T_{max,H_2O} - T_{sur})$$

$$t = -\tau_s \ln(\theta)$$

$$\theta = \frac{T - T_{sur}}{T_{max} - T_{sur}}$$

where h is the thermal conductivity, s is the laser irradiation area, T_{max} is the maximum equilibrium temperature, and T_{sur} is the ambient temperature, and Q_{dis} represents the heat dissipation from the solvent and container, while I is the laser power. A_{808} refers to the absorbance of the material at a wavelength of 808 nm. m_i is the mass of the deionized water, and C_{H_2O} is the heat capacity of deionized water (4.2 J g^{-1} $°C^{-1}$).

Hemolysis assay

Peripheral blood was collected from the veins around the eyes of BALB/c mice into anticoagulation tubes. Different concentrations of MPDA-BSA@IR780 (25, 50, and 100 μg mL^{-1}) were prepared in EP tubes. PBS was used as a negative control, and ultrapure water as a positive control, with 20 μL of peripheral blood added to each tube. The samples were incubated for 1 hour at 37 °C, then centrifuged at 2500 rpm for 5 minutes. The resulting supernatant was carefully transferred to a 96-well plate, and the absorbance at 450 nm was measured using a microplate reader. The hemolysis rate was calculated as follows: $[OD_{sample} - OD_{PBS\ group}]/[OD_{H_2O} - OD_{PBS\ group}] \times 100\%$.

Cellular uptake assay

The uptake of MPDA-BSA@IR780 by EMT6 cells was quantitatively assessed using flow cytometry. EMT6 cells (5×10^4 cells per well) were seeded into 6-well plates and incubated overnight. The original medium was then replaced with fresh medium containing MPDA-BSA@IR780 (100 μg mL^{-1}), and the cells were incubated for various time points (1, 2, 4, and 6

hours). Following incubation, cells were digested with trypsin, washed with PBS, and collected by centrifugation. The cells were resuspended in PBS, and the uptake of MPDA-BSA@IR780 was quantified by measuring the average proportion of cellular uptake using flow cytometry (ATTUNE NXT, Thermo Fisher Scientific, USA).

Evaluation of cytotoxicity and photocytotoxicity

To evaluate the toxicity and photothermal effects of MPDA-BSA@IR780, cell viability was assessed using the CCK-8 assay. EMT6 cells were seeded into 96-well plates and incubated at 37 °C in a 5% CO_2 atmosphere for 24 hours. Then, different concentrations of MPDA and MPDA-BSA@IR780 (6.25, 12.5, 25, 50, and 100 μg mL^{-1}) were added, and the cells were further incubated for 24 hours. Alternatively, after 6 hours of incubation with different concentrations of MPDA and MPDA-BSA@IR780, cells were subjected to 808 nm laser irradiation (1 W cm^{-2}) for 5 minutes, followed by an additional 24 hours incubation. To assess the biocompatibility of the nanoparticles with normal cells, Beas2b cells were incubated with various concentrations of MPDA and MPDA-BSA@IR780 (6.25, 12.5, 25, 50, and 100 μg mL^{-1}) for 24 hours. Afterward, 10 μL of CCK-8 solution was added to each well, and the cells were incubated for an additional 1 hour. Absorbance (OD) at 450 nm was measured using a microplate reader. The cell viability was calculated using the following formula: $[(OD_{\text{experimental group}} - OD_{\text{blank group}})/(OD_{\text{control group}} - OD_{\text{blank group}})] \times 100\%$.

Calcein AM/PI staining

The combined use of calcein AM and PI enables dual fluorescence staining to assess cell viability and cytotoxicity by distinguishing live and dead cells. First, EMT6 cells were seeded into 48-well plates and incubated overnight until they adhered to the surface. Then, 100 μg mL^{-1} MPDA-BSA@IR780 was added for 6 hours (with PBS as a control), followed by irradiation with an 808 nm laser at 1 W cm^{-2} for 5 minutes. The cells were then incubated for an additional 24 hours. After incubation, EMT6 cells were stained using the calcein AM/PI kit for 30 minutes, washed with PBS, and imaged under an inverted fluorescence microscope.

Tumor bearing mouse model

To study the biodistribution of MPDA-BSA@IR780, a 100 μL suspension of EMT6 cells was injected into the right flank of female BALB/c mice, and the tumors were allowed to grow until the volume reached approximately 200 mm^3. Anti-tumor treatment was initiated once the tumor volume reached approximately 100 mm^3. Tumor growth was monitored periodically using the following formula: $V = \frac{a \times b^2}{2}$, where a is the tumor length and b is the tumor width.

In vivo fluorescence imaging

EMT6 cells (1×10^5 cells per mouse) were subcutaneously inoculated into the right flank of mice. Once the tumors reached an appropriate size, 100 μL of 4 mg kg^{-1} MPDA-BSA@IR780 was administered *via* tail vein injection. Following anesthesia with sodium pentobarbital, fluorescence imaging of the mice was performed using the IVIS Lumina Series III Imaging System (PerkinElmer, Baltimore, MD, USA) at time points of 1, 4, 8, 12, and 24 hours. *In vivo* fluorescence images of the mice and the fluorescence intensity within the tumor region were analyzed using Living Image 4.5.2 software. The excitation and emission wavelengths of MPDA-BSA@IR780 were 720 nm and 790 nm, respectively.

In vivo photoacoustic imaging

To investigate the potential of MPDA-BSA@IR780 as a photoacoustic (PA) contrast agent, various concentrations of MPDA-BSA@IR780 solutions (200, 400, 800, and 1000 μg mL^{-1}) were first tested using a PA imaging system (VisualSonics, Co., Ltd). For *in vivo* PA imaging, 100 μL of 4 mg kg^{-1} MPDA-BSA@IR780 was administered *via* tail vein injection. Following anesthesia with sodium pentobarbital, photoacoustic imaging of the mice was performed at 1, 4, 8, 12, and 24 hours post-injection using the PA Imaging System (VisualSonics, Co., Ltd).

In vivo photothermal therapy

Mice with an initial tumor volume of 100 mm^3 were randomly assigned to four experimental groups: a control group, a laser group, an MPDA-BSA@IR780 group, and an MPDA-BSA@IR780 + laser group, with five mice in each group. Administration: tail vein, the dose of MPDA-BSA@IR780 was 4 mg kg^{-1}, 100 μL per mouse. Shift: every three days, four times in total. For the laser treatment groups, mice were subjected to laser irradiation (1.0 W cm^{-2}, 5 minutes) after 12 hours injection. Tumor temperature during irradiation was monitored using a thermal imager. Tumor volume and body weight were recorded throughout the treatment period. After 12 days, the mice were euthanized, and serum was collected for analysis of clinically relevant biochemical parameters. Major organs and tumors were harvested and weighed for further examination.

Histological examination

At the end of the study, all mice were euthanized, and major organs (heart, liver, spleen, lungs, kidneys) and tumors were harvested. These tissues were fixed in 4% formaldehyde solution. After fixation, the tumors and organs underwent a dehydration process, followed by embedding in paraffin. The sections were stained with hematoxylin and eosin for general histological analysis, and tumor apoptosis was evaluated using the terminal deoxynucleotidyl transferase-mediated dUTP nick end labeling (TUNEL) assay.

Statistical analysis

All results were presented as means ± standard deviation (SD). Student's *t*-test and one-way analysis of variance (ANOVA) were used to analyze statistical significance ($^*P < 0.05$, $^{**}P < 0.01$, and $^{***}P < 0.001$).

Results and discussion

Construction and characterization of MPDA-BSA@IR780

The synthesis route for MPDA-BSA@IR780 is illustrated in Fig. 1. Initially, MPDA nanoparticles were synthesized by self-polymerization under alkaline conditions, using dopamine monomer as the precursor. Next, the BSA@IR780 probe was prepared using a previously reported method,[26] and subsequently loaded into the MPDA nanoparticles to form the MPDA-BSA@IR780 composite. Field Emission Scanning Electron Microscopy (FESEM) and Transmission Electron Microscopy (TEM) images (Fig. 2a and b) revealed the morphology of the as-prepared MPDA nanoparticles, which were spherical in shape with a distinct mesoporous structure. The TEM image of MPDA-BSA@IR780 (Fig. 2c) showed that the composite particles retained a spherical morphology with an average diameter of approximately 170 nm. Energy Dispersive Spectroscopy (EDS) electron mapping (Fig. 2d and e) demonstrated a uniform distribution of C, N, and O elements across the nanoparticles, while Cl was localized within the particles. X-ray Photoelectron Spectroscopy (XPS) analysis (Fig. 2i) confirmed the presence of Cl in addition to C, N, and O, verifying the successful incorporation of BSA@IR780 into the composite. The UV-vis spectra of pure MPDA and MPDA-BSA@IR780 (Fig. 2f) showed a significant increase in absorption at 800 nm for the MPDA-BSA@IR780 nanoparticles, compared to pure MPDA, confirming the successful loading of BSA@IR780. This enhanced absorption in the NIR region indicated that the combination of MPDAand BSA@IR780 effectively improved their photothermal performance. Dynamic light scattering (DLS) analysis (Fig. 2g) revealed that the average hydrodynamic size of MPDA is 220 nm, while the hydrodynamic size of MPDA-BSA@IR780 is 230 nm, which is slightly higher than that of MPDA. The discrepancy between the TEM and DLS measurements is likely due to hydration-induced swelling observed in the DLS analysis. Additionally, the zeta potential of the nanoparticles was evaluated (Fig. 2h). The MPDA nanoparticles exhibited a zeta potential of −33.53 mV, which slightly increased to −32.1 mV after BSA@IR780 loading. The high negative charge of the MPDA-BSA@IR780 nanoparticles contributed to their excellent stability in biological environments, preventing adsorption by plasma proteins and other biomolecules. Based on the concentration standard fitting curve of IR780 (Fig. S1†), the drug loading of MPDA-BSA@IR780 was calculated to be 37.8%.

Evaluation of the fluorescence performance of MPDA-BSA@IR780

The combination of chlorine-containing cyanine dyes with proteins facilitated a distorted intramolecular charge transfer (FICT) process, significantly enhancing both the brightness and photostability of the system.[27] Due to its poor water solubility and the aggregation-caused quenching (ACQ) effect, free IR780 exhibited weak fluorescence. However, this quenching effect was notably alleviated by binding IR780 to BSA (Fig. S2†), leading to a substantial increase in fluorescence intensity (Fig. 3a and b). Furthermore, compared to IR780-loaded MPDA and MPDA alone, the MPDA-BSA@IR780 complex-incorporating BSA-coated IR780-demonstrated a significant

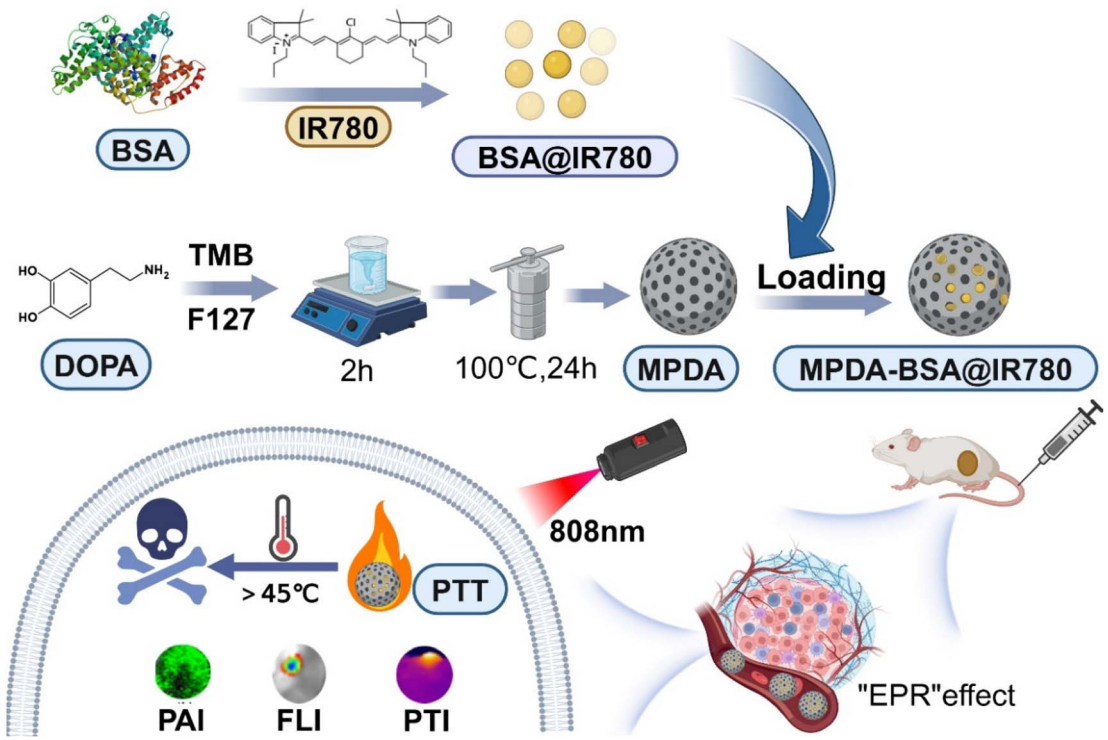

Fig. 1 Illustration of the synthesis and photothermal therapy of mesoporous polydopamine (MPDA)-BSA@IR780.

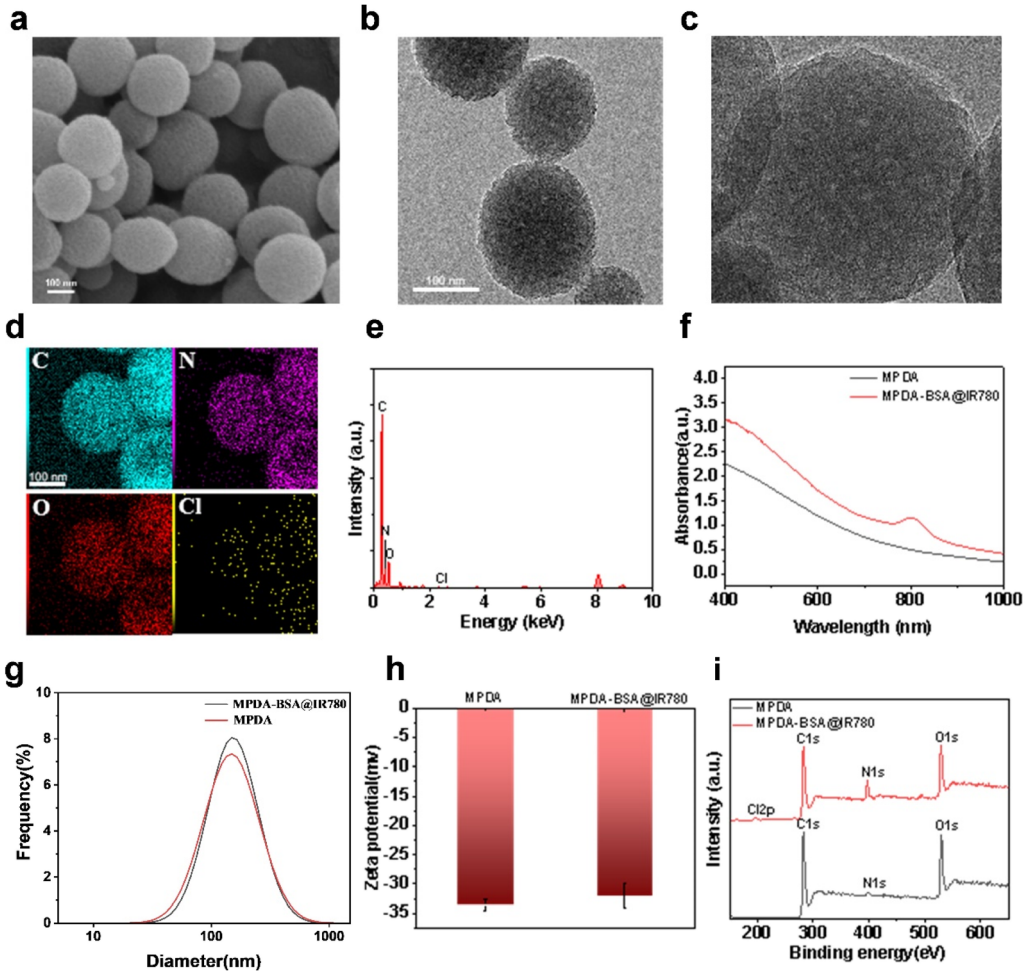

Fig. 2 (a) Field emission scanning electron microscopy (FESEM) image of MPDA. (b) Transmission electron microscopy (TEM) image of MPDA. (c) TEM image of MPDA-BSA@IR780. (d) Elemental mapping of carbon (C), nitrogen (N), oxygen (O), and chlorine (Cl) in MPDA-BSA@IR780. (e) Energy-dispersive X-ray spectroscopy (EDS) spectrum of MPDA-BSA@IR780. (f) UV-visible absorption spectra of MPDA and MPDA-BSA@IR780. (g) Hydrodynamic size distribution of MPDA and MPDA-BSA@IR780. (h) Zeta potential measurements of MPDA and MPDA-BSA@IR780. (i) X-ray photoelectron spectroscopy (XPS) full spectrum of MPDA and MPDA-BSA@IR780.

enhancement in fluorescence intensity (Fig. 3c, d and S3†), making it more suitable for fluorescence imaging applications. These results confirm the effectiveness of the protein-coating strategy, which greatly boosted the fluorescence intensity of MPDA-BSA@IR780. The photostability of free IR780, BSA@IR780, and MPDA-BSA@IR780 was also evaluated under continuous laser irradiation (Fig. 3e). The data revealed that the half-life of free IR780 was under 4 minutes, while BSA@IR780 exhibited a half-life of approximately 11 minutes. In contrast, MPDA-BSA@IR780 demonstrated exceptional photostability, with a half-life exceeding 23 minutes. Additional verification of photostability was obtained through UV-visible spectroscopy (Fig. S5†), which showed that BSA binding significantly enhanced the photostability of IR780, with further improvement achieved by using MPDA as a carrier. Finally, NIR fluorescence images of MPDA-BSA@IR780 at varying concentrations (50, 100, 200, and 400 μg mL^{-1}) were captured using the IVIS imaging system (Fig. 3f).

Assessment of the photothermal properties of MPDA-BSA@IR780

To evaluate the photothermal properties of MPDA-BSA@IR780, temperature changes were monitored using a thermal imager. The photothermal effects of both MPDA and MPDA-BSA@IR780 were quantitatively analyzed under NIR irradiation (808 nm, 1 W cm^{-2}). After continuous irradiation, the temperature of the MPDA-BSA@IR780 solution increased by 26.7 °C, MPDA showed a rise of 15.6 °C, and the aqueous solution exhibited only a slight increase of 0.6 °C (Fig. 4a). While the temperature of the BSA@IR780 solution increased by only 7.6 °C before beginning to decrease (Fig. S4†). Thermal images under NIR irradiation were also captured (Fig. 4b). These results clearly demonstrated that MPDA-BSA@IR780 exhibited a significant photothermal effect, consistent with its UV absorption spectra. Furthermore, the photothermal effect of MPDA-BSA@IR780 was found to depend on both the irradiation intensity and the concentration (Fig. 4c and d), with the temperature increase in

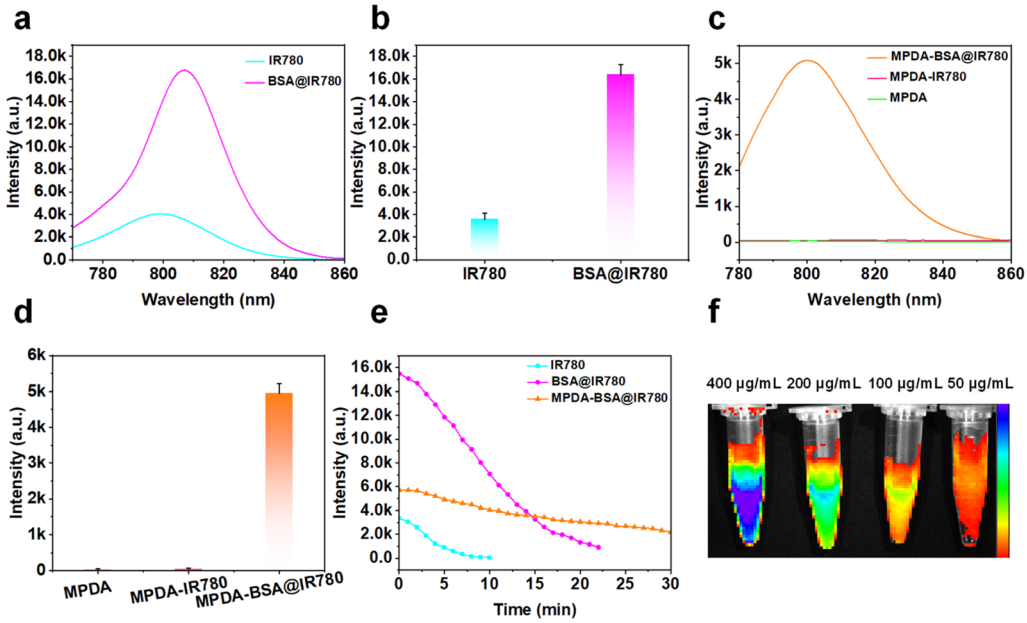

Fig. 3 (a) Fluorescence emission spectra of IR780 and BSA@IR780. (b) Comparison of fluorescence intensity between BSA@IR780 and free IR780. (c) Fluorescence emission spectra of MPDA, MPDA-IR780, and MPDA-BSA@IR780. (d) Comparison of fluorescence intensity between MPDA, MPDA-IR780, and MPDA-BSA@IR780. (e) Photostability of IR780, BSA@IR780, and MPDA-BSA@IR780 under continuous laser irradiation (808 nm, 1 W cm^{-2}). (f) Near-infrared (NIR) images of MPDA-BSA@IR780 at varying concentrations in EP tubes.

the solution correlating with higher irradiation power and concentration.

The photothermal conversion efficiency (PCE, η) of MPDA-BSA@IR780 was calculated to be 29.11% based on the initial heating–cooling cycle temperature change (Fig. 4e), while the PCE of the MPDA carrier alone was only 20.54% (Fig. S6†).

The photothermal stability of MPDA-BSA@IR780 was further assessed (Fig. 4f), demonstrating minimal temperature

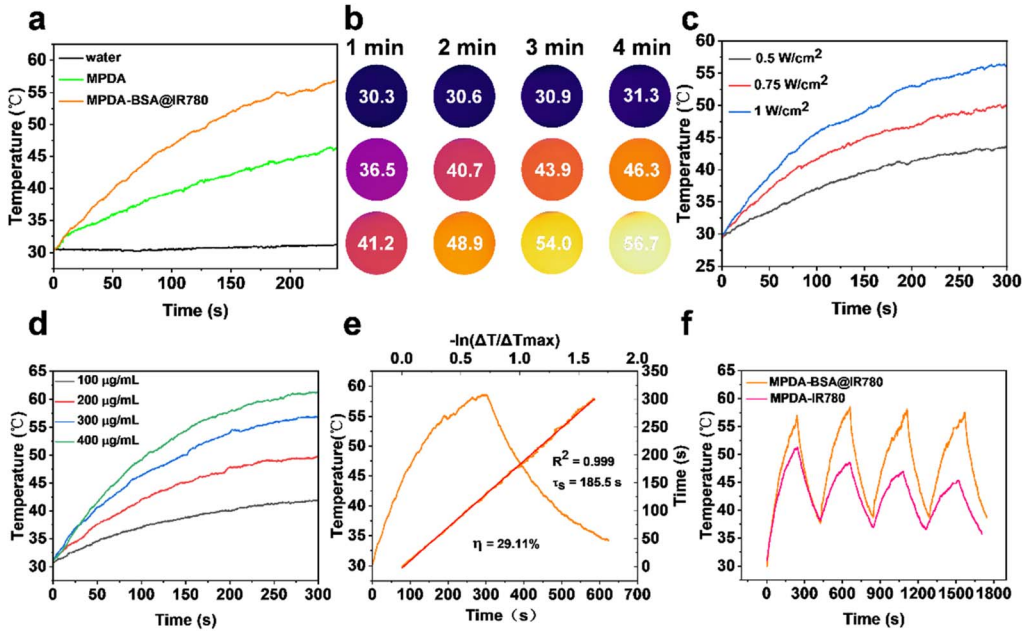

Fig. 4 (a) Temperature changes of water, MPDA, and MPDA-BSA@IR780 upon exposure to an 808 nm laser (1 W cm^{-2}). (b) Infrared thermal images of water, MPDA, and MPDA-BSA@IR780. (c) Temperature profiles of MPDA-BSA@IR780 at various power densities (0.5, 0.75, and 1.0 W cm^{-2}) under 808 nm laser irradiation. (d) Temperature profiles of MPDA-BSA@IR780 at different concentrations (100, 200, 300, and 400 μg mL^{-1}) under 808 nm laser irradiation. (e) Photothermal conversion efficiency (PCE) of MPDA-BSA@IR780 at a concentration of 300 μg mL^{-1} and an irradiation power of 1 W cm^{-2}. (f) Temperature variations of MPDA-BSA@IR780 and MPDA-IR780 during four heating and cooling cycles.

variation and high stability over four heating and cooling cycles. Additionally, the maximum temperature of MPDA did not decrease after multiple cycles (Fig. S6†), indicating that MPDA is a reliable photothermal carrier. In contrast, the temperature of the MPDA-IR780 solution gradually decreased over successive cycles, suggesting that the BSA coating on IR780 in MPDA-BSA@IR780 effectively enhanced its photothermal stability and reproducibility, thereby offering superior photostability.

In vitro cellular assays

The effective intracellular uptake of MPDA-BSA@IR780 is essential for its application in breast cancer therapy. To evaluate the cellular uptake of MPDA-BSA@IR780, EMT6 cells were incubated with the complex for various durations, and the uptake was quantified by flow cytometry (FCM). Quantitative analysis revealed that the proportion of cellular uptake increased with longer incubation times (Fig. 5a), while the percentage of cells exhibiting uptake also gradually rose (Fig. 5b), indicating efficient internalization of MPDA-BSA@IR780 into EMT6 cells *via* endocytosis. The cytotoxicity of MPDA and MPDA-BSA@IR780 in EMT6 cells was assessed using a CCK-8 assay, both with and without 808 nm laser irradiation. After 24 hours of incubation without laser treatment, both MPDA and MPDA-BSA@IR780 exhibited minimal toxicity, demonstrating good biocompatibility of both the MPDA carrier and the MPDA-BSA@IR780 formulation (Fig. 5c). To further assess biocompatibility with healthy cells, the cytotoxicity of MPDA and MPDA-BSA@IR780 was tested on Beas-2B cells, with results indicating negligible cytotoxicity (Fig. S7†). Under laser irradiation, however, MPDA-BSA@IR780 exhibited significantly higher cytotoxicity than MPDA at the same concentration (Fig. 5d). At a concentration of 100 μg mL^{-1}, 33% of the cells survived after treatment with MPDA-BSA@IR780, compared to 55% survival in cells treated with MPDA alone. These results

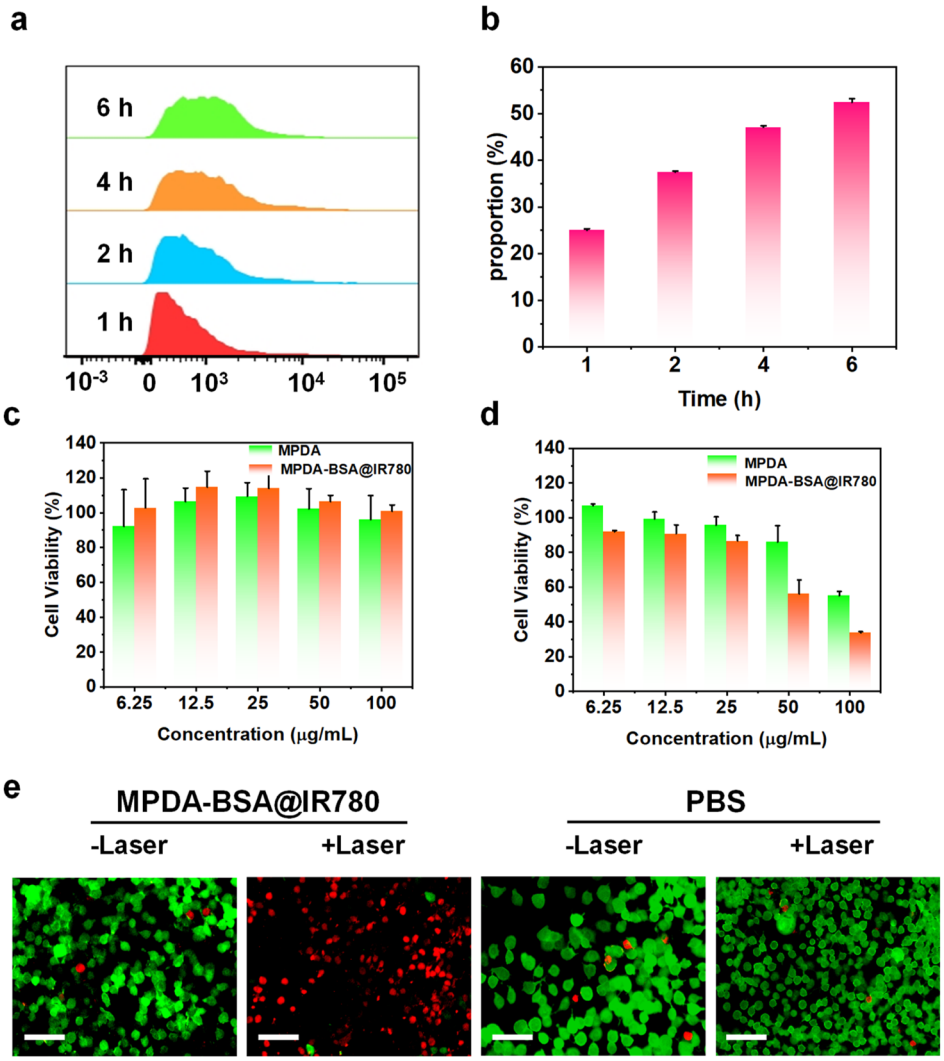

Fig. 5 (a) Flow cytometry analysis of EMT6 cells incubated with MPDA-BSA@IR780 for different time points. (b) Corresponding proportion of cellular uptake at each time point. (c) Cell viability of EMT6 cells after 24 hours of incubation without 808 nm laser irradiation. (d) Cell viability of EMT6 cells after 24 hours of incubation under 808 nm laser irradiation (1 W cm^{-2}, 5 min). (e) AM/PI live–dead double staining of EMT6 cells following treatment with PBS or MPDA-BSA@IR780 under 808 nm laser irradiation (1 W cm^{-2}, 5 min). Scale bar = 100 μm.

suggest that laser irradiation effectively enhances the photocytotoxicity of MPDA-BSA@IR780. Additionally, live–dead staining experiments using calcein AM and propidium iodide (PI) confirmed the enhanced tumoricidal activity of MPDA-BSA@IR780. As shown in Fig. 5e, cells treated with MPDA-BSA@IR780 under irradiation exhibited substantial cell death, while control cells treated with PBS showed no significant cell death, regardless of laser exposure. Unirradiated MPDA-BSA@IR780-treated cells also exhibited survival, consistent with the cytotoxicity data. Collectively, these results highlight the promising potential of MPDA-BSA@IR780 for photothermal therapy.

In vivo biodistribution experiments

Nanoprobes with imaging guidance are essential tools for enhancing therapeutic precision. To assess the distribution of MPDA-BSA@IR780 within organisms, we systematically evaluated its *in vitro* and *in vivo* PA imaging performance. The results demonstrated that the PA signal of MPDA-BSA@IR780 increased linearly with rising concentrations of the nanospheres (Fig. 6a). For *in vivo* imaging, MPDA-BSA@IR780 was intravenously administered to EMT6 tumor-bearing mice, and tumor imaging was performed at specified time points. Over time, MPDA-BSA@IR780 progressively accumulated at the tumor site, with the most pronounced signal observed at 12 hours post-injection (Fig. 6b). Notably, the PA signal intensity at 12 hours was 2.9 times higher than at 1 hour post-injection (Fig. 6c), confirming that MPDA-BSA@IR780 is an effective PA contrast agent for tumor imaging. To further validate the distribution of MPDA-BSA@IR780 *in vivo*, we assessed its tumor-targeting capability by monitoring fluorescence at the tumor site using a small animal imaging system. As shown in Fig. 6d and e, fluorescence accumulation at the tumor reached its peak at 12 hours, which aligned with the PA imaging results. Subsequently, non-specific fluorescence accumulation at other sites gradually decreased, while the fluorescence at the tumor site remained detectable for up to 24 hours. These findings not only highlight the efficient *in vivo* accumulation of MPDA-BSA@IR780 but also confirm its potential as a diagnostic imaging agent, providing accurate tumor localization information.

In vivo evaluation of the phototherapeutic efficacy

In vitro therapeutic effects of MPDA-BSA@IR780 were promising, prompting further investigation into its *in vivo* photothermal therapeutic potential. EMT6 tumor-bearing mice were randomly divided into four groups: the PBS group, the PBS + laser group, the MPDA-BSA@IR780 group, and the MPDA-BSA@IR780 + laser group. To assess the *in vivo* photothermal effect of the nanoparticles, an infrared thermal imaging system was used to record both infrared images and temperature changes at the tumor site (Fig. 7a and b). Upon intravenous injection of MPDA-BSA@IR780 followed by NIR laser irradiation (808 nm, 1 W cm^{-2}, 5 min), the temperature at the tumor site

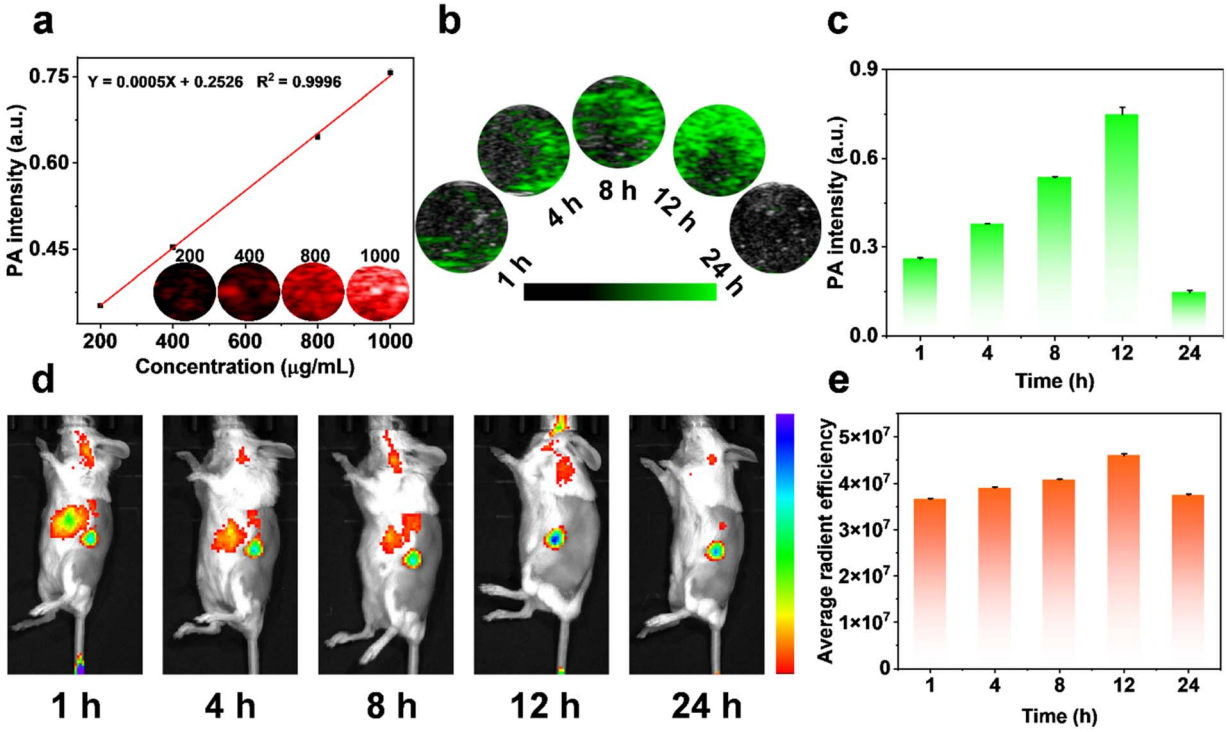

Fig. 6 (a) *In vitro* photoacoustic (PA) imaging of MPDA-BSA@IR780 at varying concentrations, along with a linear regression analysis of MPDA-BSA@IR780 concentration *versus* PA intensity. (b) PA images of tumor regions at different time points, and (c) corresponding quantitative analysis of PA intensity. (d) Fluorescence images of mice at different time intervals (1, 4, 8, 12, and 24 hours) following intravenous injection of MPDA-BSA@IR780, and (e) corresponding quantitative analysis of fluorescence intensity in the tumor region.

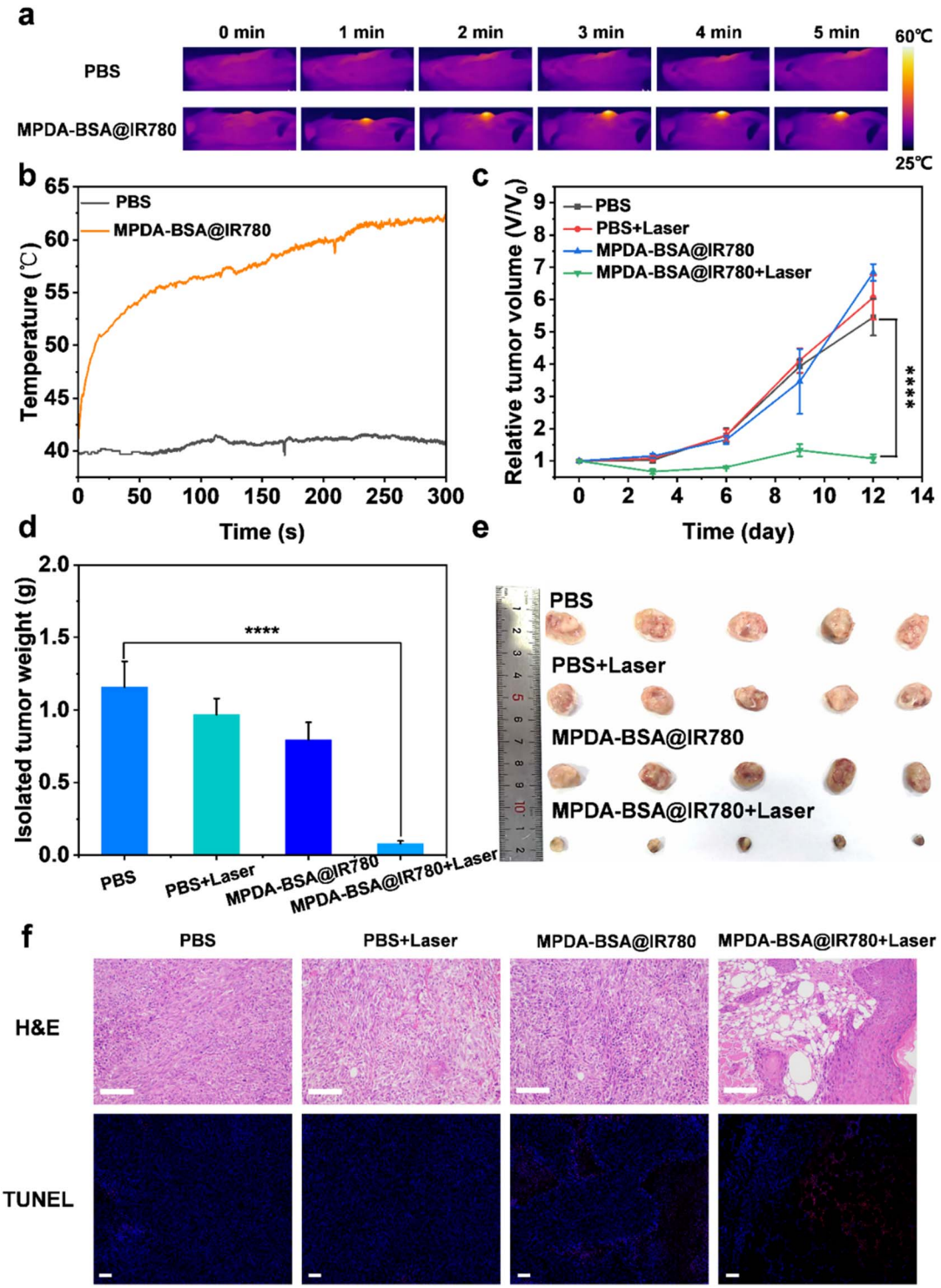

Fig. 7 (a) Thermal images of tumor-bearing mice injected with PBS or MPDA-BSA@IR780, subjected to 808 nm laser irradiation (1 W cm^{-2}, 5 min). (b) Temperature variations in tumor-bearing mice following 808 nm laser irradiation. (c) Changes in relative tumor volume in mice following different treatments. (d) Final tumor tissue weight extracted from euthanized mice 12 days post-treatment. (e) Tumor morphology observed in tissue samples from euthanized mice after 12 days of treatment. (f) H&E-stained and TUNEL-stained images of tumor sections from each treatment group, scale bar = 100 μm.

rapidly increased to 62 °C within 5 min, leading to tumor ablation. In contrast, no significant photothermal effect was observed in the PBS group, suggesting that the accumulation of MPDA-BSA@IR780 particles at the tumor site, coupled with the photostable photothermal therapy effect, is key to the observed therapeutic outcomes. To evaluate the anti-tumor effect of photothermal therapy, tumor growth was monitored in mice. Tumors in the control groups grew rapidly, while in the MPDA-

BSA@IR780 group subjected to NIR irradiation, tumor volume gradually decreased over time (Fig. 7c). This trend was further confirmed by the significant differences in tumor weight between groups (Fig. 7d) and visual inspection of isolated tumors (Fig. 7e), which collectively indicate the substantial anti-tumor effects of MPDA-BSA@IR780 combined with laser treatment. To assess the impact of photothermal therapy on tumor cell apoptosis, H&E staining and TUNEL assays were performed on resected tumor tissues. H&E-stained tumor sections from the MPDA-BSA@IR780 + laser group showed extensive cellular damage, with significant necrosis, whereas tumors from the other groups maintained well-organized structures with intact nuclei (Fig. 7f). Similarly, TUNEL staining revealed a significantly higher number of apoptotic cells in the MPDA-BSA@IR780 + laser group, further confirming the induction of apoptosis (Fig. 7f). Overall, these results suggest that MPDA-BSA@IR780, when combined with laser irradiation, provides a significant phototherapeutic effect capable of inhibiting tumor growth through hyperthermic ablation.

Safety assessment

As shown in Fig. 8a, all groups of mice exhibited a consistent increase in body weight over time, suggesting that MPDA-BSA@IR780 demonstrates good biocompatibility and low toxicity. This observation was further supported by hemolysis assays (Fig. 8b). The biosafety of the treatment groups was also evaluated through serum biochemical and routine blood assays.

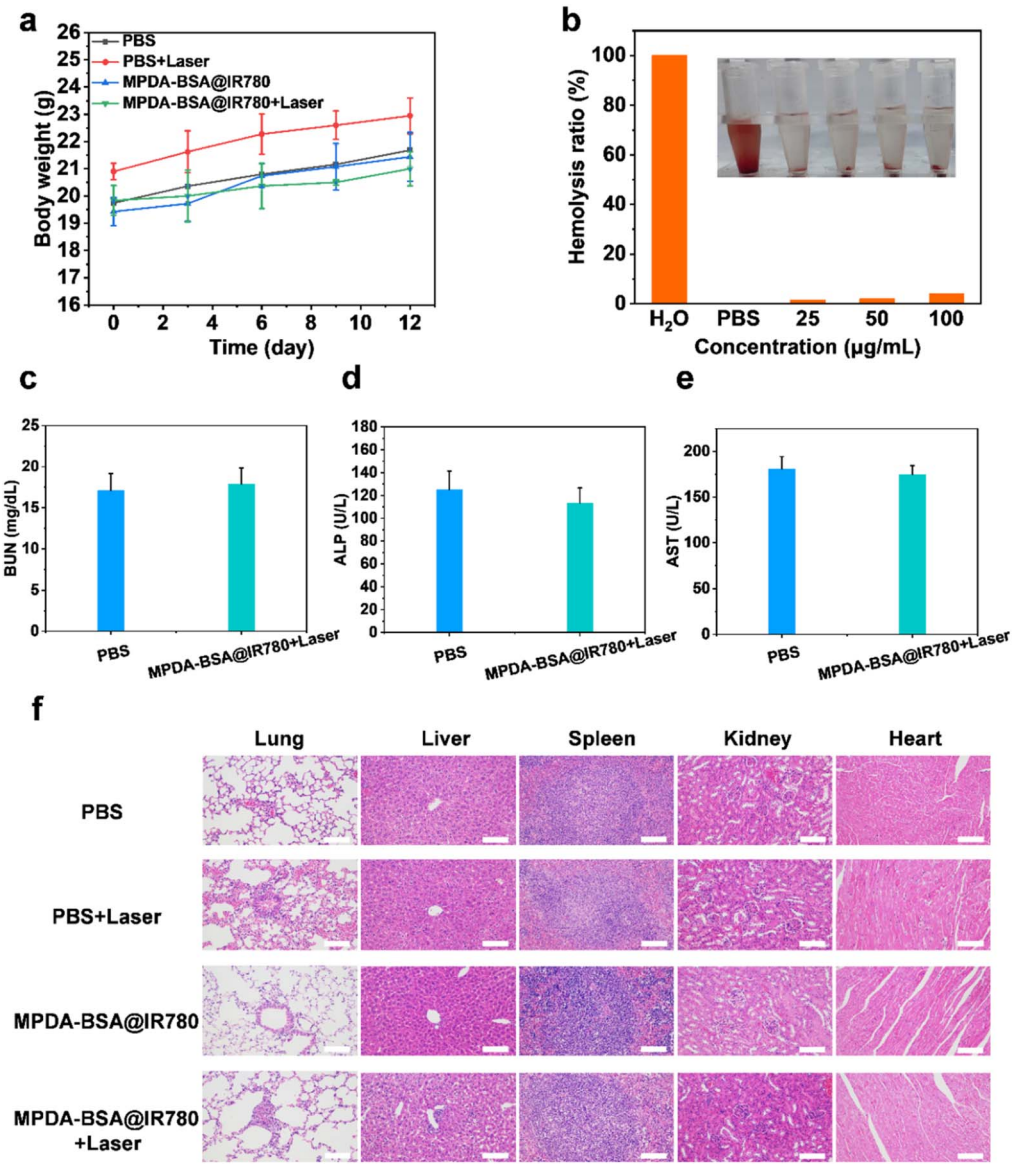

Fig. 8 (a) Changes in the body weight of mice over 12 days following different treatments. (b) Blood safety assessment for various concentrations of MPDA-BSA@IR780. (c–e) Serum biochemical analyses of blood urea nitrogen (BUN), alkaline phosphatase (ALP), and aspartate transaminase (AST). (f) Hematoxylin and eosin (H&E) staining images of the main organs (heart, liver, spleen, lungs, kidneys) in tumor-bearing mice after different treatments, scale bar = 100 μm.

No significant differences were observed between the PBS and MPDA-BSA@IR780 + laser groups in terms of serum levels of blood urea nitrogen (BUN), alkaline phosphatase (ALP), and aspartate transaminase (AST), as well as blood cell parameters such as plateletcrit (PCT), mean corpuscular hemoglobin concentration (MCHC), and granulocyte (Gran) (Fig. 8c–e, and S8†). To assess the potential effects of MPDA-BSA@IR780 on organ health, tissues from the heart, liver, spleen, lungs, and kidneys of each mouse were dissected and stained with hematoxylin and eosin (H&E) (Fig. 8f). Notably, the MPDA-BSA@IR780-treated group exhibited results similar to the control group, with almost no observable lesions in the organs, indicating that MPDA-BSA@IR780 has favorable biosafety for *in vivo* use and does not adversely affect the morphology of major organs. Collectively, these findings demonstrate that MPDA-BSA@IR780 possesses excellent biocompatibility and holds promise for potential therapeutic applications.

Conclusions

In summary, we successfully developed a new multifunctional diagnostic nanoplatform, MPDA-BSA@IR780, for PA/FL dual imaging-guided photothermal therapy. This nanosphere, which was uniformly sized and structurally stable, could efficiently accumulate in tumor tissues. Notably, compared to MPDA-IR780, the incorporation of BSA reduced the self-quenching effect of IR780, enhancing the photostability and fluorescence imaging capabilities of MPDA-BSA@IR780. Additionally, combining the MPDA carrier with the BSA@IR780 probe optimized their individual strengths, facilitating the construction of an integrated diagnostic platform. When compared to MPDA, MPDA-BSA@IR780 exhibited a higher photothermal effect, overcoming the limited photothermal capability of BSA@IR780. Under laser irradiation, temperature exceeding 55 °C was sufficient to induce tumor cell death. Furthermore, the MPDA carrier improved fluorescence stability, providing an extended imaging window. Both *in vitro* and *in vivo* treatments with MPDA-BSA@IR780 yielded excellent results, including superior imaging performance. Biosafety assessments, including blood biochemical tests and histological analysis, confirmed the good biocompatibility of MPDA-BSA@IR780. Therefore, we believe that MPDA-BSA@IR780 held significant potential for tumor therapy and offered promising new perspectives for multifunctional tumor diagnosis and treatment. We anticipated that the development of other therapeutic nanoplatforms with diverse structures and mechanisms would further enhance the clinical translation potential of such technologies.

Data availability

The data that support the findings of this study are available from the corresponding author upon reasonable request.

Author contributions

Shuaibo Yang: investigation, formal analysis, methodology, conceptualization, visualization, writing – original draft, writing review & editing. Yanzhao Diao: investigation, formal analysis, methodology, conceptualization, visualization, writing – original draft, writing – review & editing. Lifeng Hang: investigation, methodology, visualization, writing – review & editing. Hong Qu, Laiping Fang, Wei Guo, KuokWai IU: investigation, methodology, visualization. Guihua Jiang, Lianyi Shao, Quan Li: resources, writing – original draft, writing review & editing, visualization, funding acquisition.

Conflicts of interest

There are no conflicts to declare.

Acknowledgements

This work was supported by the National Natural Science Foundation of China (2022YFC2410000, 82371913, and 82271948), Distinguished Youth Program of the Guangdong Second Provincial General Hospital (2024D003), Guangzhou Key Laboratory of Molecular Functional Imaging and Artificial Intelligence for Major Brain Diseases (20220102037320), Guangzhou Women and Children's Medical Center (2019BS025), and the Foundation of Guangzhou Health Science and Technology Project (20221A011030).

References

1 Z. Zhang, W. Xu, M. Kang, H. Wen, H. Guo, P. Zhang, L. Xi, K. Li, L. Wang, D. Wang and B. Z. Tang, *Adv. Mater.*, 2020, **32**, 2003210.
2 Z. Yan, B. Song, G. Fang, T. Wu, N. Chen, M. Zhao, X. Zou and G. Liao, *ACS Sustain. Chem. Eng.*, 2021, **9**, 10403–10423.
3 S. Guan, X. Liu, Y. Fu, C. Li, J. Wang, Q. Mei, G. Deng, W. Zheng, Z. Wan and J. Lu, *J. Colloid Interface Sci.*, 2022, **608**, 344–354.
4 Y. Liu, P. Bhattarai, Z. Dai and X. Chen, *Chem. Soc. Rev.*, 2019, **48**, 2053–2108.
5 L. Zhang, Y. Liu, H. Huang, H. Xie, B. Zhang, W. Xia and B. Guo, *Adv. Drug Delivery Rev.*, 2022, **190**, 114536.
6 C. Li, Y. Cheng, D. Li, Q. An, W. Zhang, Y. Zhang and Y. Fu, *Int. J. Mol. Sci.*, 2022, **23**, 7909.
7 C. Li, Y. Xu, L. Tu, M. Choi, Y. Fan, X. Chen, J. L. Sessler, J. S. Kim and Y. Sun, *Chem. Sci.*, 2022, **13**, 6541–6549.
8 X. Qi, Y. Huang, S. You, Y. Xiang, E. Cai, R. Mao, W. Pan, X. Tong, W. Dong, F. Ye and J. Shen, *Adv. Sci.*, 2022, **9**, 2106015.
9 R. Taheri-Ledari, F. Ganjali, S. Zarei-Shokat, R. Dinmohammadi, F. R. Asl, A. Emami, Z. S. Mojtabapour, Z. Rashvandi, A. Kashtiaray, F. Jalali and A. Maleki, *Nanoscale Adv.*, 2023, **5**, 6768–6786.
10 B. Lü, Y. Chen, P. Li, B. Wang, K. Müllen and M. Yin, *Nat. Commun.*, 2019, **10**, 767.
11 G.-H. Lu, W.-T. Shang, H. Deng, Z.-Y. Han, M. Hu, X.-Y. Liang, C.-H. Fang, X.-H. Zhu, Y.-F. Fan and J. Tian, *Biomaterials*, 2019, **195**, 13–22.
12 X. Li, J. Shan, W. Zhang, S. Su, L. Yuwen and L. Wang, *Small*, 2017, **13**, 1602660.

13 H. S. Han and K. Y. Choi, *Biomedicines*, 2021, **9**, 305.
14 H. Zhang, X. Chen, S. Li, J. Shen and Z.-W. Mao, *Molecules*, 2022, **27**, 2629.
15 T. Nagy-Simon, M. Potara, A. M. Craciun, E. Licarete and S. Astilean, *J. Colloid Interface Sci.*, 2018, **517**, 239–250.
16 X. Cui, X. Deng, Z. Liang, J. Lu, L. Shao, X. Wang, F. Jia, Z. Pan, Q. Hu, X. Xiao, Y. Wu and W. Sheng, *Biomater. Sci.*, 2021, **9**, 3838–3850.
17 G. Jo, E. J. Kim and H. Hyun, *Int. J. Mol. Sci.*, 2023, **24**, 862.
18 R. Tian, Q. Zeng, S. Zhu, J. Lau, S. Chandra, R. Ertsey, K. S. Hettie, T. Teraphongphom, Z. Hu, G. Niu, D. O. Kiesewetter, H. Sun, X. Zhang, A. L. Antaris, B. R. Brooks and X. Chen, *Sci. Adv.*, 2019, **5**, eaaw0672.
19 L. Bai, Z. Hu, T. Han, Y. Wang, J. Xu, G. Jiang, X. Feng, B. Sun, X. Liu, R. Tian, H. Sun, S. Zhang, X. Chen and S. Zhu, *Theranostics*, 2022, **12**, 4536–4547.
20 B. Du, C. Qu, K. Qian, Y. Ren, Y. Li, X. Cui, S. He, Y. Wu, T. Ko, R. Liu, X. Li, Y. Li and Z. Cheng, *Adv. Opt. Mater.*, 2020, **8**, 1901471.
21 M. Li, Z. Luo and Y. Zhao, *Chem. Mater.*, 2018, **30**, 25–53.
22 H. Zhuang, M. Zhao, S. Ding, L. Liu, W. Yuan, L. Jiang, X. Han, L. Jiang and T. Yi, *ACS Appl. Mater. Interfaces*, 2020, **12**, 38906–38917.
23 R. Mrówczyński, *ACS Appl. Mater. Interfaces*, 2018, **10**, 7541–7561.
24 Z. Wang, Y. Duan and Y. Duan, *J. Controlled Release*, 2018, **290**, 56–74.
25 Y. Zhou, B. Xu, P. Zhou, X. Chen, G. Jiao and H. Li, *Int. J. Biol. Macromol.*, 2023, **253**, 127441.
26 J. Xu, Y. Du, T. Han, N. Zhu and S. Zhu, *Adv. Healthcare Mater.*, 2023, **12**, 2301051.
27 C. Wang, Q. Qiao, W. Chi, J. Chen, W. Liu, D. Tan, S. McKechnie, D. Lyu, X.-F. Jiang, W. Zhou, N. Xu, Q. Zhang, Z. Xu and X. Liu, *Angew. Chem., Int. Ed.*, 2020, **59**, 10160–10172.